Journal of *Imaging*

MDPI

Article

In-Situ Imaging of Liquid Phase Separation in Molten Alloys Using Cold Neutrons †

Nicholas Alexander Derimow [1,‡], Louis Joseph Santodonato [2,*,‡], Rebecca Mills [2] and Reza Abbaschian [1]

[1] Materials Science and Engineering, University of California, Riverside, CA 92521, USA; nderimow@engr.ucr.edu (N.A.D.); rabba@engr.ucr.edu (R.A.)

[2] Neutron Scattering Division, Oak Ridge National Laboratory, Oak Ridge, TN 37830, USA; millsra@ornl.gov

* Correspondence: santodonatol@ornl.gov; Tel.: +1-865-719-0656

‡ These authors contributed equally to this work.

Received: 31 October 2017; Accepted: 7 December 2017; Published: 25 December 2017

Abstract: Understanding the liquid phases and solidification behaviors of multicomponent alloy systems becomes difficult as modern engineering alloys grow more complex, especially with the discovery of high-entropy alloys (HEAs) in 2004. Information about their liquid state behavior is scarce, and potentially quite complex due to the presence of perhaps five or more elements in equimolar ratios. These alloys are showing promise as high strength materials, many composed of solid-solution phases containing equiatomic CoCrCu, which itself does not form a ternary solid solution. Instead, this compound solidifies into highly phase separated regions, and the liquid phase separation that occurs in the alloy also leads to phase separation in systems in which Co, Cr, and Cu are present. The present study demonstrates that in-situ neutron imaging of the liquid phase separation in CoCrCu can be observed. The neutron imaging of the solidification process may resolve questions about phase separation that occurs in these alloys and those that contain Cu. These results show that neutron imaging can be utilized as a characterization technique for solidification research with the potential for imaging the liquid phases of more complex alloys, such as the HEAs which have very little published data about their liquid phases. This imaging technique could potentially allow for observation of immiscible liquid phases becoming miscible at specific temperatures, which cannot be observed with ex-situ analysis of solidified structures.

Keywords: neutron imaging; in-situ imaging; alloys; phase separation; solidification; medium entropy alloys; high entropy alloys; multicomponent element alloys

1. Introduction

The continuous search for better engineering alloys has given rise to the superalloys, bulk metallic glasses, and more recently, the high-entropy alloys (HEAs), also referred to as complex concentrated alloys (CCAs), and multiprincipal element alloys (MPEAs). Introduced in 2004, a "high-entropy" alloy was first considered to be an equiatomic combination of 3 to 5 elements that form a single-phase solid solution, with a large configurational entropy of mixing [1–6]. The definition has since been relaxed somewhat, as researchers have been synthesizing these alloys with many components in non-equiatomic combinations to form dual-phase materials and intermetallic compounds.

Enormous efforts have been made to understand their potential as engineering materials as many of the 3d transition metal HEAs/CCAs/MPEAs are comparable to austenitic steels, precipitation hardened steels, austenitic nickel alloys, and other superalloy classes—many having non-equiatomic 3d transition metal combinations which can be classified as CCAs [7]. To harness the potential of these alloys, researchers must reliably understand the thermodynamics and formation mechanisms of these materials during various processing routes. It is extremely difficult to visualize the hyperdimensional phase diagrams of multicomponent alloys containing more than 3 base elements, and efforts have been made to accelerate the discovery of single-phase HEAs by using computational methods [8–10]. These methods are useful for refining the search for single-phase and dual-phase HEAs, and along with experimental studies of new HEA systems, the field is moving in the direction of getting a better understanding of how these alloys form. However, information about HEA behavior in the liquid state is scarce, specifically pertaining to liquid phase separation and the presence of miscibility gaps.

In the recent review by Miracle et al., approximately 85% of all HEAs thus far contained the 3d transition metals Co, Cr, Cu, Fe, Mn, Ni, Ti, V, as well as Al [7]. Out of these 3d transition metal HEAs, approximately 33% of the 345 alloys contain equiatomic CoCrCu, which has been shown to form no ternary compound, instead shows a very large liquid phase miscibility gap and upon solidification leads to Cu-lean and Cu-rich phases [11]. In order to investigate the possible liquid phase separation in more complex alloys such as the HEAs in Reference [7], in-situ studies of liquid phase separation in "medium entropy" alloy CoCrCu were carried out to verify that the technique can identify distinct phase-separated liquids, which in turn can be applied to the other CoCrCu-containing systems. This work would provide a novel characterization technique for investigating the thermodynamics and phase formation mechanics of new and existing metals used throughout industry.

Liquid phase separation has been recorded in many alloy systems such as Co-Cu [12–18], Cu-Fe [19–24] Cu-Nb [17,25], Co-Cr-Cu [11], and Co-Cu-Fe [17,26–28]. More recently, Munitz et al. show that HEA systems CoCrCuFe, CoCrCuFeNiNb, CoCrCuFeV, CoCrCuFeTi$_{0.5}$V, CoCrCuFeTiV, and CrCuFeMnV undergo stable liquid phase separation into Cu-rich and Cu-lean phases [29]. The previous experiments have not measured real time liquid phase separation, but rather the resultant microstructures of the Cu-rich and Cu-lean phases. Many of the HEAs in the literature contain Co, Cr, and Cu and have distinct regions that are rich in Cu, examples of which being the alloys in Table 1. As the field of HEAs continues to grow, the understanding of phase formation and separation will continue to be problematic as these alloys phase diagrams will be very complex. Post-mortem analysis can sometimes lead to difficulty when trying to understand how certain phases form, therefore using cold neutrons to image a solidification process can potentially lead to better understanding of the solidification behavior of the alloy in question.

Table 1. High-entropy alloys (HEAs) studied in the literature that contain equiatomic CoCrCu with Cu-rich phase separation.

HEA	References
CoCrCuFeMn	[30]
CoCrCuFeNi	[29,31–34]
CoCrCuFeMnNiTiV	[35]
CoCrCuFeMoNi	[36]
CoCrCuFeNiTi	[37]

In-situ neutron imaging provides a unique opportunity to image liquid phase separation in the form of a carefully constructed sequence of neutron radiographs throughout sample heating and cooling. This technique could be utilized to provide insight into bulk molten alloy behavior, and can potentially be used for studying solid state phases which subsequently form and whether macro separation takes place. Real-space imaging with ~80 μm spatial resolution, sufficient to see

globule-like separation in materials such as the present CoCrCu alloys, (where the phase separation can be on the order of 200+ μm [11]), is routinely available at several neutron user facilities worldwide.

Although the spatial resolution of neutron imaging instruments will continue to become more precise, other significant challenges may arise when combining standard neutron imaging capabilities with the in situ heating and melting of an alloy as crucible size, furnace distance to the detector, and dimensions of the detector will influence the amount of sample that can be melted.

The neutron transmission through the elements used in this study (Table 2) is suitable for studying phase separation within mm-size crucibles. The neutron transmission values are calculated based upon the expression,

$$I(\lambda) = I_0(\lambda)e^{-\mu(\lambda)\Delta x}$$

where $I(\lambda)$ and $I_0(\lambda)$ are the transmitted and incident neutron intensities, respectively, for the wavelength λ, and path length Δx, through the attenuating material. The wavelength-dependent attenuation coefficient $\mu(\lambda)$, is given by

$$\mu(\lambda) = \sigma_{tot}(\lambda)\frac{\rho N_A}{M},$$

where $\sigma_{tot}(\lambda)$ is the total (adsorption plus scattering) neutron cross section of the material, ρ is the mass density, N_A is Avogadro's number, and M is the molar mass [38].

The neutron wavelengths for the present study were in the "cold" range, with a distribution peaking at about 2.6 Å. Thus, for the purpose of estimating transmission and contrast among the elements, a fixed value of λ = 2.6 Å was used in the equation above. The densities ρ and molar masses, M, of the room-temperature metals were used in the calculations.

Table 2. Table of neutron transmission through the elements, and the CoCr-rich phase, used in this study.

Composition	Density (g/cm^3)	Transmission Δx = 4 mm	Transmission Δx = 8 mm
Co	8.9	12%	1%
Cr	7.2	77%	59%
Cu	9.0	63%	40%
CoCr	8.0	31%	10%

Indications of liquid phase separation can be deduced by the difference in contrast of the regions inside the melt. Due to the elements in Table 2 having different neutron transmission percentages, it is predicted that the different phases can be distinguished from the other, as the CoCrCu melt separates into Cu-rich and Cu-lean liquids. Liu et al. provided an experimental determination and thermodynamic calculation for the CoCrCu system where a stable liquid phase miscibility gap of Cu-rich and Cu-lean liquids should exist at 1500 °C, especially in near-equiatomic concentrations of each element in the melt [11].

2. Materials and Methods

2.1. Sample Preparation and Microstructural Characterization

Identical samples of CoCrCu were prepared with elemental purity of Co $\geq$ 99.9%, Cr $\geq$ 99.99%, and Cu $\geq$ 99.9%. Each sample weighing approximately 1.5 g and was acr-melted three times (flipped twice) on a water-cooled Cu hearth in a Ti-gettered argon atmosphere. Sample dimensions were semi-spherical buttons (Figure 1a) and were approximately 6 mm in diameter and 3–4 mm tall. For microstructural characterization, an arc-melted button of CoCrCu was electromagnetically levitated and remelted to temperatures within the liquid miscibility gap (1130–1630 °C). After visual

confirmation that the system was molten, the sample was cast onto a flat Cu surface from ~1500 °C. Sample melting was also confirmed due to the flat (coin-like) shape of the splat sample not retaining any of the spherical shape of an arc-melted button. Temperature of the alloy system was recorded with a Metis M3 2-color pyrometer with temperature range of (500 to 1800 °C). The flat cast sample was cut vertically in half using a diamond wafering blade and subsequently mounted face down in BPA epoxy resin. The mounted sample was then abraded using SiC paper up to 1200 grit, and polished using 1 μ, 0.3 μ and 0.05 μ Al_2O_3 powder. Backscattered electron images and energy dispersive X-ray spectroscopy (EDS) of the mounted sample were obtained with a NovaNanoSEM 450 scanning electron microscope (FEI Company, Hillsboro, OR, USA). Another arc-melted button was also cut in half with a diamond wafering blade and polished for optical microscopy.

2.2. Furnace Setup and Sample Installation

Samples of CoCrCu were placed in alumina crucibles (Figure 1a), attached to a Nb mounting adaptor with alumina screws, and attached to the sample stick (Figure 1b) of a top-loading vacuum furnace. Although the sample was securely held within the crucible, it was not sealed, and thus shared the same vacuum space as the furnace. The dimensions of the crucibles were 27 mm tall, 8 mm inner diameter, and 12 mm outer diameter. The crucible lid was approximately 13 mm in diameter with a 3 mm height. The stick was lowered into the "ILL-type" furnace, originally developed at the Institut Laue-Langevin, and sealed to the vacuum chamber (Figure 1c). This furnace was customized at Oak Ridge National Laboratory, including the Nb-foil heating elements, heat shields, and control system, for operation up to 1500 °C with the present samples (Figure 2). The furnace was continually pumped during heating to maintain the vacuum of ~1×10^{-6} mbar.

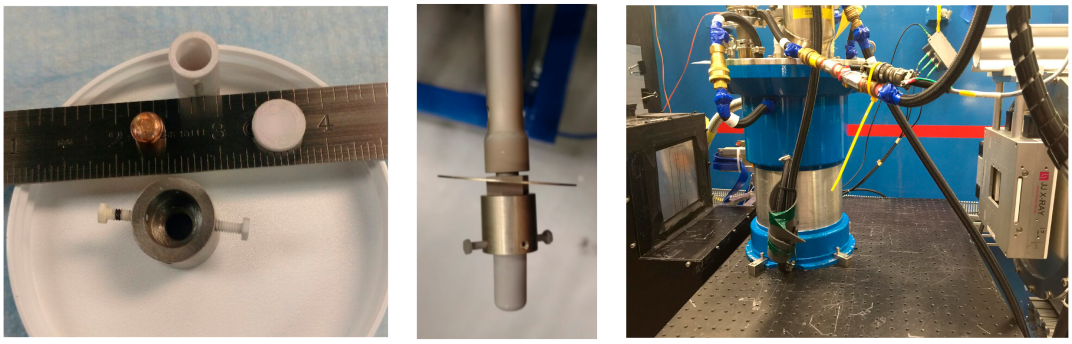

(**a**) (**b**) (**c**)

Figure 1. Images of the experimental setup at the CG-1D beamline at the High Flux Isotope Reactor (HFIR) at Oak Ridge National Laboratory. (**a**) Sample of CoCrCu, Al_2O_3 crucible, lid, and Nb mounting adaptor placed near a ruler for scale. (**b**) The crucible mounted to the sample stick. (**c**) The high-vacuum Institut Laue-Langevin (ILL) furnace placed between the detector and incident neutron beam slits.

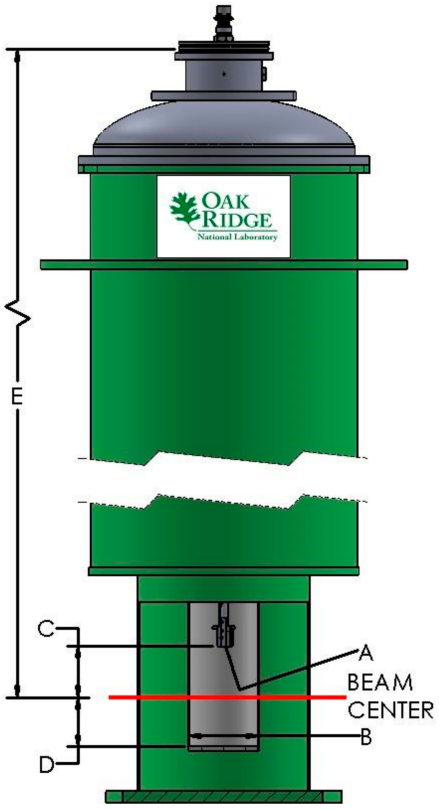

Figure 2. ILL Niobium Foil Vacuum Furnace. Temperature range of 30–1500 °C (A) Interface connection M8 × 1.25 (male) (B) Bore size diameter = 50 mm (C) Distance interface to beam center = 31.75 mm (D) Beam center to sample space bottom = 11.862 cm (E) Distance stick flange to beam center = 41.275 cm. Image of ILL furnace "HOT-A" courtesy of Oak Ridge National Laboratory Sample Environment Group.

2.3. Neutron Imaging

The CG-1D Neutron Imaging Instrument at Oak Ridge National Laboratory uses a polychromatic "cold" neutron beam, obtained by passing the beam through a liquid hydrogen cold source, giving a wavelength range of $0.8 < \lambda < 6$ Å, peaking at 2.6 Å. As the neutron beam enters the CG-1D instrument, it passes through one of four user-selectable circular apertures with diameters, D = 3.3, 4.1, 8.2, 11, or 16 mm. This set of apertures allows users to make the tradeoff between higher neutron flux (larger D), or greater spatial resolution (greater L/D ratio, where L = 6.59 m is the distance between the aperture and detector). The intermediate aperture size of 8.2 mm was chosen for the present furnace work, where the large sample-to-detector distance (~20 cm) caused significant image blurring with large apertures. The present detector assembly is capable of 80 μm spatial resolution. The working resolution, however, changes depending upon the experimental configuration. Under the present experimental setup, the working resolution was ~200 μm, because the sample-to-detector distance is relatively large (~20 cm) when using the furnace. This resolution degradation was mitigated by choosing a relatively small aperture (8.2 mm). The scintillators are routinely changed among different thicknesses (25, 50, and 100 μm). The 50 μm thickness was used for the present work. The detector field-of-view (FOV) is a 75 mm square region on the scintillator screen. The working FOV of the sample slightly decreases from 75 mm with sample-to-detector distance, according to a 2-degree beam divergence.

Neutron radiographs were acquired using a ^{6}LiF/ZnS scintillator viewed by a CCD detector with 20, 40, and 55 s, exposure times for the various heating curves described below. The heterogeneous alloy of CoCrCu was inserted into the furnace for heating. The image acquisition was set to acquire 5 images every 50 °C from 900–1500 °C with a 1 °C tolerance and ramp rate of 17 °C/min. Each image

was acquired for 40 s, and the images were only captured once 1 °C tolerance had been reached for each temperature. At the maximum temperature of 1500 °C, 10 images were taken before the temperature script entered the cooling. Ten dark field and ten open beam images were acquired under the same conditions for image normalization. Computed tomography (CT) scans were carried out at room temperature of the samples inside the crucible on a rotating stage from 0 to 183° in steps of 0.20° at a rate of 1 image/step and an exposure time of 55 s per image (~14 h scan).

This in situ heating process was refined with two samples of CoCrCu stacked inside the small style alumina crucible in Figure 1a so that the flow of liquids toward the crucible bottom could be observed. The stacked sample system is what is discussed throughout the rest of the text. The image acquisition for the stacked CoCrCu system was refined to produce a more movie-like series of radiographs, and therefore set to acquire 10 images every 25 °C from 900–1500 °C with a 5 °C tolerance and ramp rate of 17 °C/min. Each image was acquired for 20 s in order to maintain good resolution while maintaining the same time (200 s) at each temperature before the continuing in the heating curve. This allowed for more images to be captured at each temperature of the heating curve (Figure 3) while maintaining enough resolution to distinguish between the separated liquid phases. At the maximum temperature of 1500 °C, 20 images were taken before the script entered the cooling portion of the curve. This temperature of the system can be seen in Figure 3. After the sample cooled, computed tomography (CT) scans were again carried out at room temperature of the solid in the crucible on a rotating stage from 0 to 183° in steps of 0.20° at a rate of 1 image/step and an exposure time of 55 s per image (~14 h scan). The images were then normalized in the standard fashion, by subtracting the dark field from the raw images, and dividing by (open beam-dark field) radiographs.

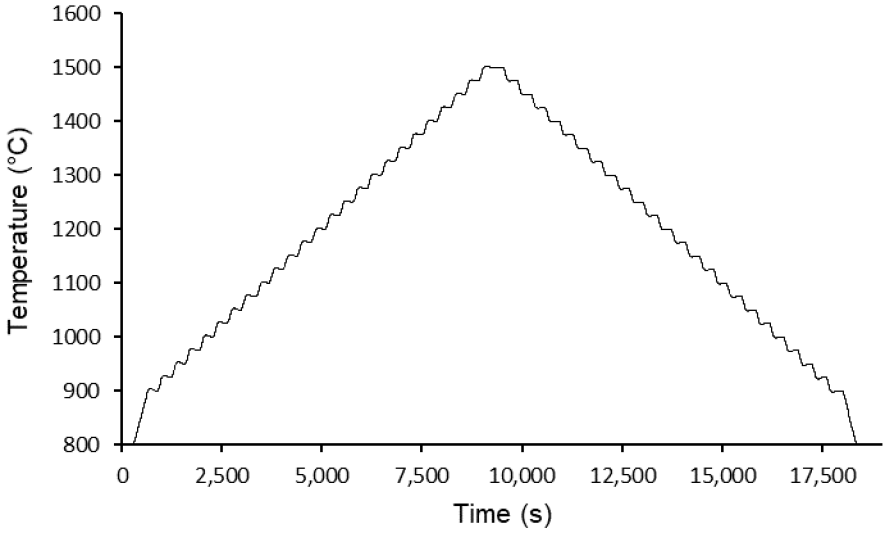

Figure 3. Temperature vs. time of the stacked CoCrCu system heating from 900 to 1500 °C and back to 900 °C in 25 °C increments.

3. Results

3.1. Microstructural Characterization Using Electron Microscopy

The ex situ microstructural characterization of the levitated sample revealed Cu-rich and Cu-lean phases, as seen in Figure 4a by the different colored grayscale regions. The amount of electrons that are scattered back to the detector is proportional to the atomic number of the material (brighter regions~higher Z), therefore, the brighter region at the top is a Cu-rich phase (2.8% Co, 1.2% Cr, and 96.0% Cu), while the bottom region is Cu-lean, containing ≥90% CoCr (45.6% Co, 46.6% Cr, and 7.8% Cu), confirmed by energy dispersive X-ray spectroscopy (EDS). The bottom dark-gray region of the micrograph in Figure 4a displays a CoCr-rich phase that appears to solidify first, with small

dendrites seen protruding into the lighter Cu-rich region. According to the isothermal phase diagram in Reference [11], the CoCr-rich liquid solidifies first resulting in the eutectic (Cr) + (αCo) phases near equiatomic concentrations. Figure 4b displays an optical micrograph of an arc-melted button of CoCrCu. This button was cross-sectioned vertically, and the two distinct phases can be seen, represented by the different colored regions. The Cu-phase retains its distinct orange color and can be seen in along the edges of Figure 4b.

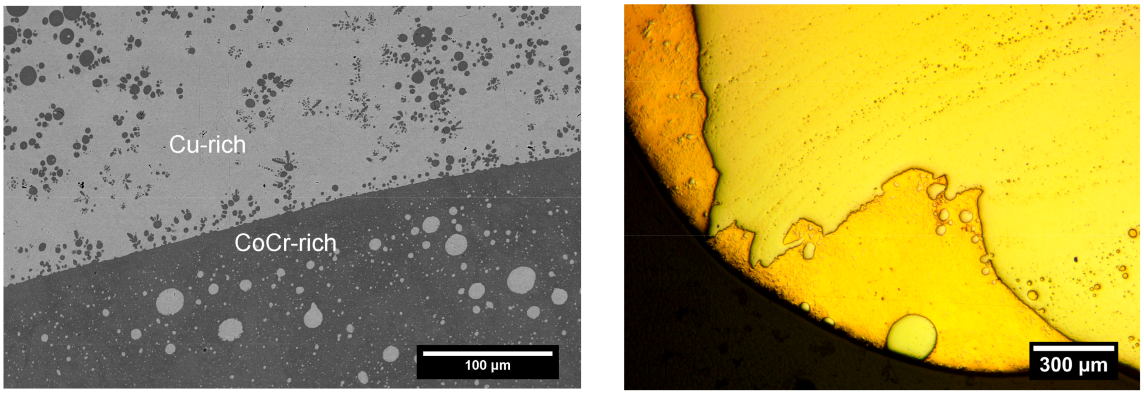

(**a**) (**b**)

Figure 4. (**a**) Backscattered electron image of CoCrCu displaying 2 distinct phases: Cu-rich (top), CoCr-rich (bottom). Note, tiny black spots are pores generated from the initial grinding/polishing process. (**b**) Optical micrograph of the bottom-half cross-section of an arc-melted CoCrCu button.

Maps of atomic composition were collected for the distinct regions, revealing the large phase separation between the Cu-rich and CoCr-rich liquids, and can be seen in Figure 5. The globule-like separation is indicative of liquid phase separation, as seen in the previous work on these and similar alloys with stable liquid miscibility gaps [11,29]. In energy dispersive X-ray mapping, each element emits a characteristic X-ray upon electrons returning to the ground state, therefore this technique allows for analysis of specific atomic concentrations of specific areas within a sample. This can be seen in Figure 5a,b where the cobalt and chromium maps correspond to the CoCr-rich region, while the separated spheres to the left are mostly copper (Figure 5c). The total elemental map is present in Figure 5d, displaying an equal mixed presence of Co and Cr, while the red Cu sphere is its own separated phase.

3.2. Neutron Imaging

For the initial imaging, a solitary CoCrCu was placed inside of the furnace and heated to 1500 °C and cooled according to the step function described for this system in the methods section. Additional experiments were conducted with two samples stacked inside the crucible (Figure 6) so that a more drastic flow can be observed. The CoCrCu sample itself does not form a solid solution with the alloying elements Co, Cr, and Cu, in contrast to some HEAs containing these elements [2]. The arc-melted CoCrCu buttons have a random distribution of Cu-rich globules that solidify alongside of the CoCr-rich species. Due to this alloy's nature for phase separation, it was the ideal candidate for neutron imaging as the Cu-rich species has a higher neutron transmission than the CoCr-rich liquid. As can be seen in Figure 6, the distribution of the Cu-rich species inside of the sample button is identified as the lighter region of the spherical shapes, as Cu allows for more transmission of neutrons compared to much darker CoCr-rich regions (Figure 6).

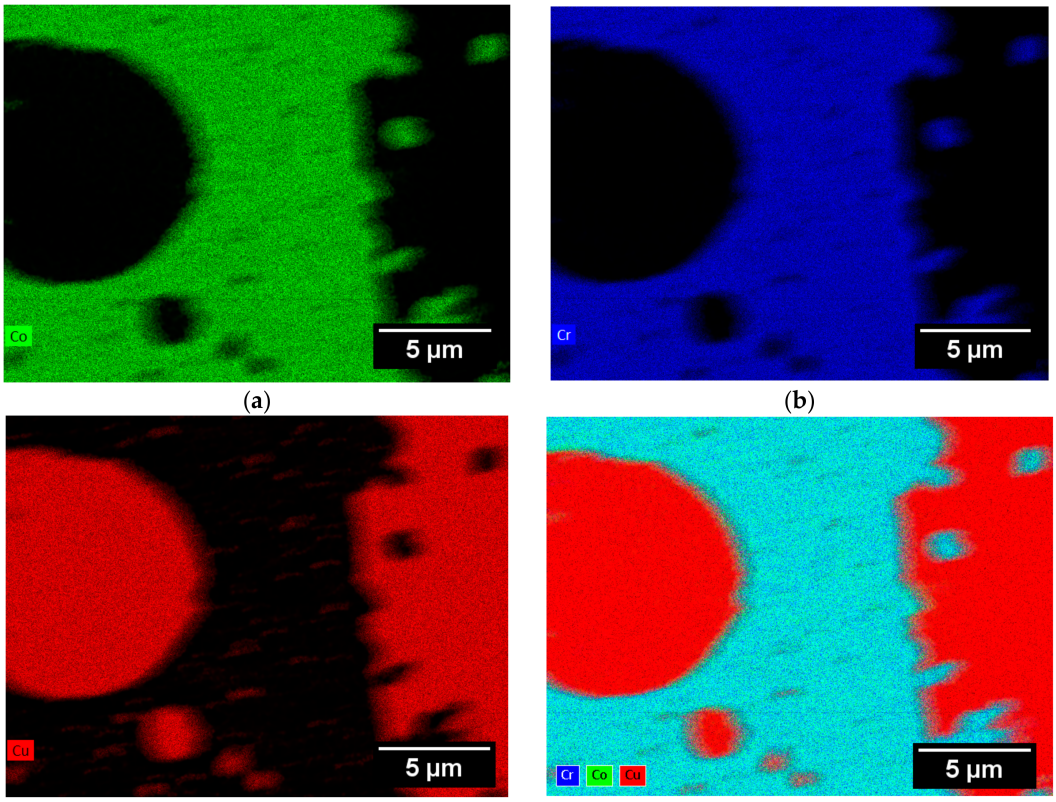

Figure 5. Energy dispersive X-ray spectroscopy (EDS) maps of the phase separated regions of the electromagnetically levitated and cast CoCrCu alloy. The colored regions correspond to the atomic composition present in the material: (**a**) Cobalt only (**b**) Chromium only (**c**) Copper only (**d**) Map of all elements in the system.

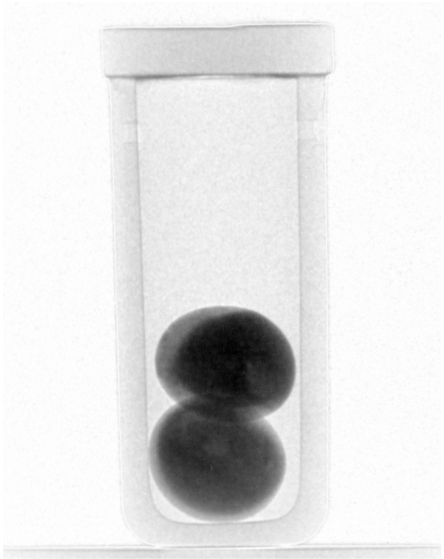

Figure 6. Room temperature radiograph of two heterogeneous arc-melted CoCrCu samples stacked inside a small crucible. The lighter regions are the Cu-rich phase (>95%) and are segregated to the surface of the buttons as well as randomly distributed globules inside the bulk. The darker regions are Co-Cr-rich and make up the rest of the arc-melted button.

The stacked CoCrCu samples in Figure 7 show two heterogeneous buttons of CoCrCu placed inside of the alumina crucible and radiographed from 900 to 1500 °C (and eventually back to 900 °C). The brighter Cu-rich regions in the 2 buttons are the first to melt and travel downward due to gravity until the CoCr-rich dark region melts and collapses into a single liquid held together by surface tension. The remaining Cu-rich (lighter phase) inside of the CoCr-rich liquid can be seen travelling out towards the top of the system, possibly as a pocket trapped by the surrounding CoCr-rich solid/liquid. Once the system was allowed to reach equilibrium, this lighter region disappears and could have made its way to the bottom of the crucible either along the sides or through the CoCr-rich liquid due to the different liquid densities. As the system reaches overall solidification, a void grows from the bottom left of the crucible. This void expands as Cu-rich liquid contracts until a low enough temperature is ultimately reached, allowing for the solidification of the Cu-rich phase (Figure 8).

As heating proceeds to overall sample melting in Figure 7, the lighter-appearing Cu-rich region flows from the sides of the buttons to the bottom of the crucible. The two liquids remain separated in the molten state until solidification of the higher melting point species. The first to solidify is the CoCr-rich region as it cools from 1500 °C and contracts next to the Cu-rich liquid (Figure 8) in between 1400 and 1350 °C, as inferred by the CoCr binary phase diagram and the isothermal sections of the CoCrCu ternary diagrams [11]. As the environment is cooled down to 900 °C the Cu-rich liquid solidifies between 1100 and 1075 °C and we are left with the two distinctly separated regions in Figure 8. Overall, two types of phase separations have been directly observed using neutron imaging. At the highest temperatures, above the liquidus, Cu-rich and Cu-lean liquids co-exist.

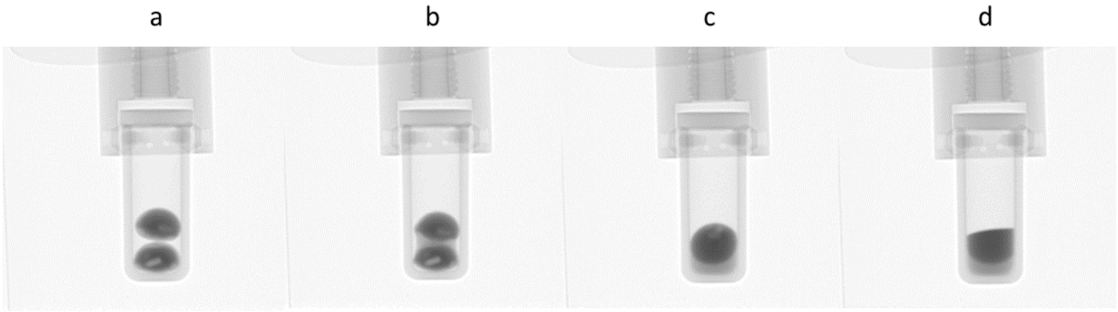

Figure 7. Melting and liquid phase separation of stacked CoCrCu samples. (**a**) During initial heating, the two as-cast buttons are intact. (**b**) The Cu-rich phase melts first between 1075 and 1100 °C, and (**c**) pools at the bottom of the crucible. (**d**) The Cu-lean phase fully melts upon heating to 1500 °C. Full video available in the supplemental.

4. Discussion

4.1. Microstructure

The microstructure and macrosegregation of CoCrCu from Figure 4 displays the Cu-rich and Cu-lean phases described previously by [11]. During the initial arc-melting, the alloy either formed a single phase liquid and underwent decomposition into two distinct liquids, or there existed a stable liquid phase separation overall throughout the melt. There is currently no literature for this ternary system regarding the miscibility gap past 1627 ºC detailing the presence of a single phase liquid, however with higher temperatures it may be possible to image approximately where this demixing occurs with cold neutrons. Further experimentation is needed to understand the thermodynamics of the CoCrCu system. The two liquids appear to remain immiscible throughout melting and solidify independently of the other, indicating the presence of a stable miscibility gap and is agreement with the miscibility gap studies of Liu et al. [11].

4.2. Neutron Imaging

In Figure 7, as temperature increases, the entire system becomes molten and reaches a thermodynamic equilibrium with a stable liquid phase miscibility gap containing Cu-rich and Cu-lean liquids. The difference in brightness between the two liquids is consistent with the expected phase separation, the brighter being the Cu-rich liquid (see Table 2, where the neutron transmission through Cu is about twice that of CoCr mixture). The phase separation is also consistent with the relative volumes, inferred from the bright versus dark image areas, such that the Cu-rich region accounts for one third of the volume determined by analyzing the areas from the CT scans with image processing software. The phase diagram suggests that the solidification of the CoCr-liquid will have a very small solubility with Cu, and vice-versa [11]. As the concentrations of the elements in the system are in equal parts, it is easy to see the separated Cu-liquid correspond to its approximate volume fraction of 1/3rd, which was verified with image analysis software (ImageJ v. 1.50b, National Institutes of Health (NIH), Bethesda, MA, USA). A final confirmation was made by visual inspection of the sample as they are copper-rich on the surface, retaining the color of pure copper, as seen in Figure 1a. As shown in Table 2, the Cu-rich and CoCr-rich species have enough contrast to be able to determine the phases based on volume fraction.

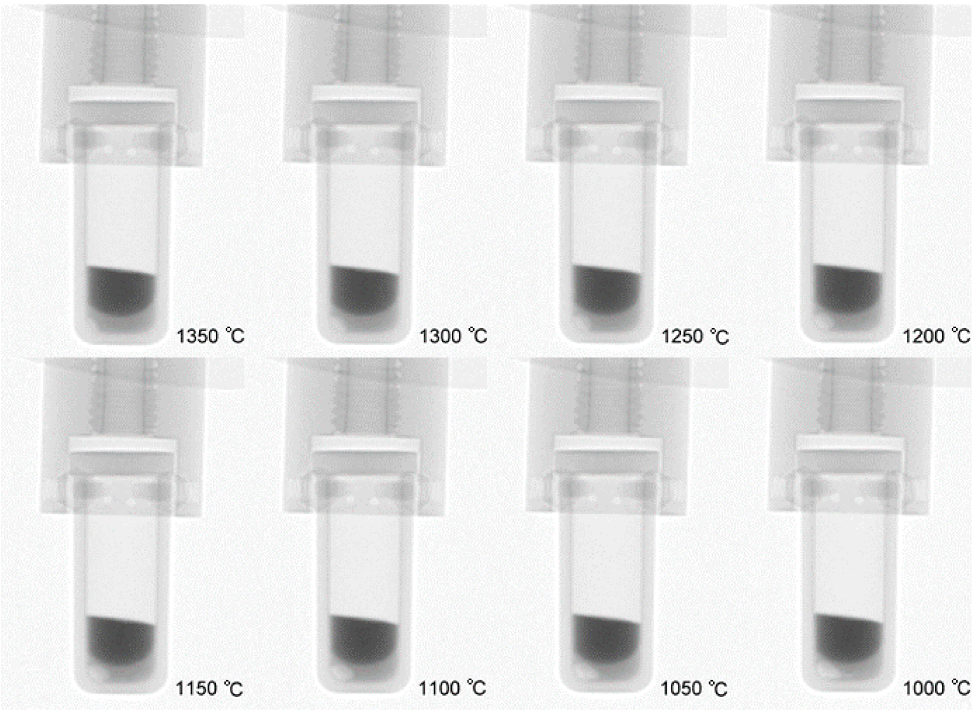

Figure 8. Cooling, macroscopic void formation, and solidification.

The neutron radiography experiments conducted on the stacked CoCrCu button display an optimized number of radiographs and temperature steps to capture a representative melt-solidification process. Figure 7 displays specific radiographs taken from the overall collection of images which forms a movie of 500 images, which can be found in the supplemental. The movie of the melting and solidification process is formatted to play at 10 frames per second (fps), such that each second displays a 25 °C step. The Cu that surrounded the surface of the button melts first and flows to the bottom of the crucible. The Co-Cr rich center collapses and forms a spherical shape in Figure 7c, likely due to surface tension of the liquid. As the temperature was increased to 1500 °C, both liquid phases were present within the miscibility gap of the system and the temperature was held for 200 s until entering the cooling portion of the temperature curve.

At 1350 °C, a void began to grow into the molten pool of Cu-rich liquid at the bottom of the crucible which can be observed in Figure 8. The void continued to grow as the Cu-rich liquid solidified between 1050 and 1000 °C. The radiograph of solidified system at room temperature and photograph of the void can be seen in Figure 9. The reconstructed computed tomography is present in Figure 10, where the Cu-rich phase is represented by the green while the CoCr-rich phase is atop in red.

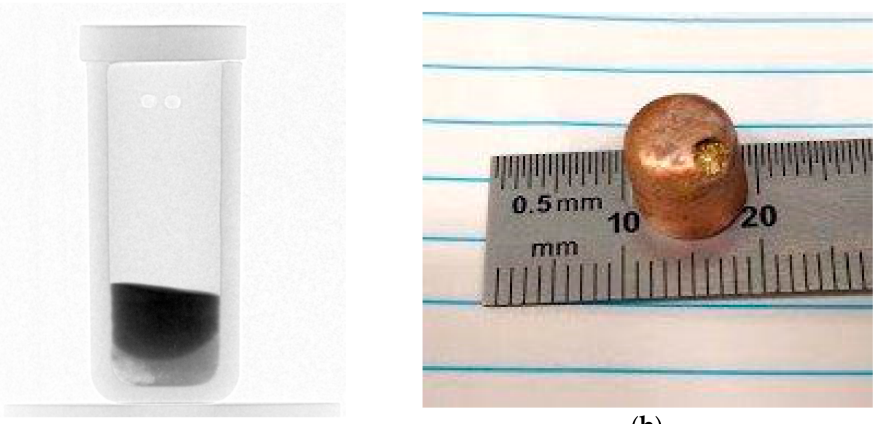

(**a**) (**b**)

Figure 9. (**a**) Room temperature radiograph of CoCrCu after the melt cycle. The darkest region atop is the Co-Cr-rich phase, while the lighter region to the bottom right was the formation of a void. The lighter gray region toward the bottom right is the Cu-rich phase. (**b**) Photograph of the sample after removal from the crucible, displaying the void that formed during solidification.

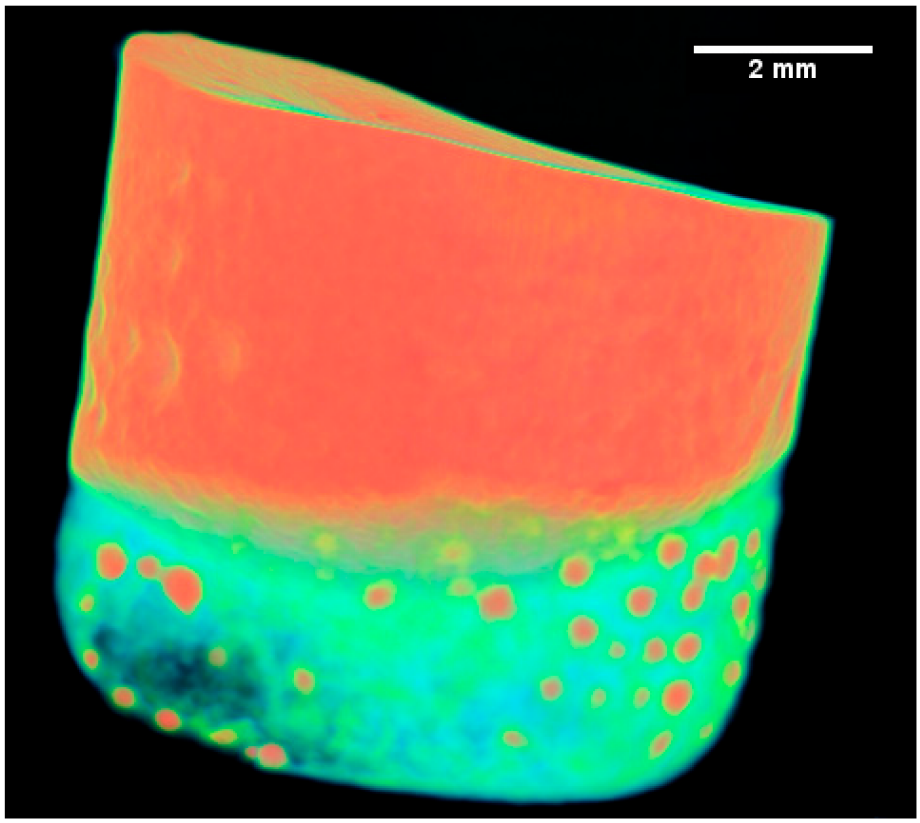

Figure 10. Reconstructed computed tomography of the CoCrCu system with void present in the bottom left, and CoCr-rich (red) globules dispersed throughout Cu-rich (green) phase.

5. Conclusions

With the growing number of complex alloy systems being studied, understanding their liquid behavior becomes crucial when designing materials for applications across industries. During casting processes, it is very hard to distinguish liquid phase separation, as most metals are not transparent. By utilizing cold neutron imaging, liquid phase separation of the CoCrCu system was able to be observed, demonstrating that this technique can be applied to other metal systems provided that the neutron transmission of the alloying elements are dissimilar enough to see a contrast between the multiple phases. This technique has the potential to be improved for future work, for example, by utilizing a smaller furnace with better transparency for neutrons such that the sample is closer to the detector with better resolution. This technique also provides a way to potentially image casting processes by constructing crucibles that simulate various cast shapes. After solidification has finished, the use of computed tomography (CT) can be applied with the cold neutrons and a rotating sample stage to look for impurities or voids within the cast. This method can be applied to study fundamental liquid state behavior in complex alloy systems, such as the high-entropy alloys. By using neutron imaging of the liquid phase, it can provide invaluable information about the alloy system as well as other systems that contain miscibility gaps and is not solely specific to liquid metals.

Supplementary Materials: The following are available online at www.mdpi.com/2313-433X/4/1/5/s1, Video of stacked system melting and solidification related to Figure 6.

Acknowledgments: Electron microscopy and microanalysis were performed on SEM device NovaNanoSEM 450 at the Central Facility for Advanced Microscopy and Microanalysis (CFAMM) at the University of California, Riverside. Neutron imaging carried out at the CG-1D Neutron Imaging Instrument at Oak Ridge National Laboratory in Oak Ridge (ORNL), Tennessee. Sample environment setup and support at ORNL was provided by Robby (Robert) Marrs and Jeff Burks. Jean Bilheux wrote data analysis scripts using Python Jupyter notebooks. Andre Parizzi, Indu Dhiman, and Hassina Bilheux provided experiment setup and support at CG-1D. This experiment was conducted during the X-ray and Neutron Summer School, held annually at the ORNL and Argonne National Laboratories. The participating students who provided insightful comments and questions included Stephanie Carpenter, Saptarshi Chakraborty, Kai Gong, Erik Hadland, Ryan Kastilani, Tyson Lanigan-Atkins, Jennifer Morey, Eve Mozur, Benjamin Palmer, Aly Rahemtulla, and Yadu Krishnan Sarathchandran.

Author Contributions: Nicholas A. Derimow, Louis J. Santodonato, and Reza Abbaschian conceived and designed the experiments; Nicholas A. Derimow and Louis J. Santodonato performed the experiments, analyzed the data, contributed reagents/materials/analysis tools, and wrote the paper. Rebecca Mills designed and constructed custom sample environment hardware, conducted extensive offline testing prior to the neutron experiment, and contributed to the Materials and Methods section of the manuscript.

Conflicts of Interest: The authors declare no conflict of interest.

References

1. Cantor, B.; Chang, I.T.H.; Knight, P.; Vincent, A.J.B. Microstructural development in equiatomic multicomponent alloys. *Mater. Sci. Eng. A* **2004**, *375*, 213–218. [CrossRef]
2. Yeh, J.-W.; Chen, S.-K.; Lin, S.-J.; Gan, J.-Y.; Chin, T.-S.; Shun, T.-T.; Tsau, C.-H.; Chang, S.-Y. Nanostructured High-Entropy Alloys with Multiple Principal Elements: Novel Alloy Design Concepts and Outcomes. *Adv. Eng. Mater.* **2004**, *6*, 299–303. [CrossRef]
3. Yeh, J.-W.; Lin, S.-J.; Chin, T.-S.; Gan, J.-Y.; Chen, S.-K.; Shun, T.-T.; Tsau, C.-H.; Chou, S.-Y. Formation of simple crystal structures in Cu-Co-Ni-Cr-Al-Fe-Ti-V alloys with multiprincipal metallic elements. *Metall. Mater. Trans. A* **2004**, *35*, 2533–2536. [CrossRef]
4. Hsu, C.; Yeh, J.; Chen, S.; Shun, T. Wear resistance and high-temperature compression strength of Fcc CuCoNiCrAl0.5Fe alloy with boron addition. *Metall. Mater. Trans. A* **2004**, *35*, 1465–1469. [CrossRef]
5. Chen, T.K.; Wong, M.S.; Shun, T.T.; Yeh, J.W. Nanostructured nitride films of multi-element high-entropy alloys by reactive DC sputtering. *Surf. Coat. Technol.* **2005**, *200*, 1361–1365. [CrossRef]
6. Huang, P.; Yeh, J.-W.; Shun, T.-T.; Chen, S.-K. Multi-Principal Element Alloys with Improved Oxidation and Wear Resistance for Thermal Spray *Coating*. *Adv. Eng. Mater.* **2004**, *6*, 74–78. [CrossRef]
7. Miracle, D.B.; Senkov, O.N. A critical review of high entropy alloys and related concepts. *Acta Mater.* **2017**, *122*, 448–511. [CrossRef]

8. Senkov, O.N.; Miller, J.D.; Miracle, D.B.; Woodward, C. Accelerated exploration of multi-principal element alloys for structural applications. *Comput. Coupling Phase Diagrams Thermochem.* **2015**, *50*, 32–48. [CrossRef]
9. King, D.J.M.; Middleburgh, S.C.; McGregor, A.G.; Cortie, M.B. Predicting the formation and stability of single phase high-entropy alloys. *Acta Mater.* **2016**, *104*, 172–179. [CrossRef]
10. Toda-Caraballo, I.; Rivera-Díaz-del-Castillo, P.E.J. A criterion for the formation of high entropy alloys based on lattice distortion. *Intermetallics* **2016**, *71*, 76–87. [CrossRef]
11. Liu, X.J.; Jiang, Z.P.; Wang, C.P.; Ishida, K. Experimental determination and thermodynamic calculation of the phase equilibria in the Cu–Cr–Nb and Cu–Cr–Co systems. *J. Alloys Compd.* **2009**, *478*, 287–296. [CrossRef]
12. Nishizawa, T.; Ishida, K. The Co-Cu (Cobalt-Copper) system. *J. Phase Equilib.* **1984**, *5*, 161–165. [CrossRef]
13. Munitz, A.; Abbaschian, R. Two-melt separation in supercooled Cu-Co alloys solidifying in a drop-tube. *J. Mater. Sci.* **1991**, *26*, 6458–6466. [CrossRef]
14. Munitz, A.; Elder-Randall, S.P.; Abbaschian, R. Supercooling effects in Cu-10 Wt Pct Co alloys solidified at different cooling rates. *Metall. Trans. A* **1992**, *23*, 1817–1827. [CrossRef]
15. Zhang, Y.K.; Gao, J.; Nagamatsu, D.; Fukuda, T.; Yasuda, H.; Kolbe, M.; He, J.C. Reduced droplet coarsening in electromagnetically levitated and phase-separated Cu-Co alloys by imposition of a static magnetic field. *Scr. Mater.* **2008**, *59*, 1002–1005. [CrossRef]
16. Zhang, Y.K.; Gao, J.; Yang, C.; Kolbe, M.; Binder, S.; Herlach, D.M. Asynchronous crystallization behavior of Co-rich droplets in phase-separated Cu-Co alloys. *Mater. Lett.* **2012**, *73*, 56–58. [CrossRef]
17. Munitz, A.; Venkert, A.; Landau, P.; Kaufman, M.J.; Abbaschian, R. Microstructure and phase selection in supercooled copper alloys exhibiting metastable liquid miscibility gaps. *J. Mater. Sci.* **2012**, *47*, 7955–7970. [CrossRef]
18. Zhang, Y.; Gao, J.; Yasuda, H.; Kolbe, M.; Wilde, G. Particle size distribution and composition in phase-separated Cu75Co25 alloys under various magnetic fields. *Scr. Mater.* **2014**, *82*, 5–8. [CrossRef]
19. Chuang, Y.Y.; Schmid, R.; Chang, Y.A. Thermodynamic analysis of the iron-copper system I: The stable and metastable phase equilibria. *Metall. Trans. A* **1984**, *15*, 1921–1930. [CrossRef]
20. Munitz, A. Metastable liquid phase separation in tungsten inert gas and electron beam copper/stainless-steel welds. *J. Mater. Sci.* **1995**, *30*, 2901–2910. [CrossRef]
21. Yamauchi, I.; Irie, T.; Sakaguchi, H. Metastable liquid separation in undercooled Fe-Cu and Fe-Cu-Si melts containing a small B concentration and their solidification structure. *J. Alloys Compd.* **2005**, *403*, 211–216. [CrossRef]
22. Chen, Y.Z.; Liu, F.; Yang, G.C.; Xu, X.Q.; Zhou, Y.H. Rapid solidification of bulk undercooled hypoperitectic Fe-Cu alloy. *J. Alloys Compd.* **2007**, *427*, 3–7. [CrossRef]
23. Curiotto, S.; Battezzati, L.; Johnson, E.; Palumbo, M.; Pryds, N. The liquid metastable miscibility gap in the Cu-Co-Fe system. *J. Mater. Sci.* **2008**, *43*, 3253–3258. [CrossRef]
24. Zhang, J.T.; Wang, Y.H.; Cui, X. C.; Lin, J.B. The growth and congregation of minor phase in immiscible Cu-Fe alloys. *Medziagotyra* **2013**, *19*, 373–376. [CrossRef]
25. Ellis, T.W.; Anderson, I.E.; Downing, H.L.; Verhoeven, J.D. Deformation-processed wire prepared from gas-atomized Cu-Nb alloy powders. *Metall. Trans. A* **1993**, *24*, 21–26. [CrossRef]
26. Munitz, A.; Abbachian, R.; Cotler, C.; Shacham, C. Liquid Phase Separation in Cu-Co-Fe and Cu-Fe-Ni-Cr Alloys. *High Temp. Mater. Process.* **1996**, *15*, 187–194. [CrossRef]
27. Kim, D. I.; Abbaschian, R. The metastable liquid miscibility gap in Cu-Co-Fe alloys. *J. Phase Equilib.* **2000**, *21*, 25–31. [CrossRef]
28. Cao, C.-D.; Görler, G.P. Direct Measurement of the Metastable Liquid Miscibility Gap in Fe–Co–Cu Ternary Alloy System. *Chin. Phys. Lett.* **2005**, *22*, 482–484.
29. Munitz, A.; Kaufman, M. J.; Abbaschian, R. Liquid phase separation in transition element high entropy alloys. *Intermetallics* **2017**, *86*, 59–72. [CrossRef]
30. Otto, F.; Yang, Y.; Bei, H.; George, E.P. Relative effects of enthalpy and entropy on the phase stability of equiatomic high-entropy alloys. *Acta Mater.* **2013**, *61*, 2628–2638. [CrossRef]
31. Park, N.; Watanabe, I.; Terada, D.; Yokoyama, Y.; Liaw, P.K.; Tsuji, N. Recrystallization Behavior of CoCrCuFeNi High-Entropy Alloy. *Metall. Mater. Trans. A* **2015**, *46*, 1481–1487. [CrossRef]
32. Liu, N.; Wu, P.H.; Zhou, P.J.; Peng, Z.; Wang, X.J.; Lu, Y.P. Rapid solidification and liquid-phase separation of undercooled CoCrCuFexNi high-entropy alloys. *Intermetallics* **2016**, *72*, 44–52. [CrossRef]

33. Wang, W.L.; Hu, L.; Luo, S.B.; Meng, L.J.; Geng, D.L.; Wei, B. Liquid phase separation and rapid dendritic growth of high-entropy CoCrCuFeNi alloy. *Intermetallics* **2016**, *77*, 41–45. [CrossRef]
34. Wu, P.H.; Liu, N.; Zhou, P.J.; Peng, Z.; Du, W.D.; Wang, X.J.; Pan, Y. Microstructures and liquid phase separation in multicomponent CoCrCuFeNi high entropy alloys. *Mater. Sci. Technol.* **2016**, *32*, 576–580. [CrossRef]
35. Zhou, Y.J.; Zhang, Y.; Wang, Y.L.; Chen, G.L. Microstructure and compressive properties of multicomponent Alx(TiVCrMnFeCoNiCu)100-x high-entropy alloys. *Mater. Sci. Eng. A* **2007**, *454*, 260–265. [CrossRef]
36. Wu, P. H.; Liu, N.; Yang, W.; Zhu, Z. X.; Lu, Y. P.; Wang, X. J. Microstructure and solidification behavior of multicomponent CoCrCuxFeMoNi high-entropy alloys. *Mater. Sci. Eng. A* **2015**, *642*, 142–149. [CrossRef]
37. Wang, X.F.; Zhang, Y.; Qiao, Y.; Chen, G.L. Novel microstructure and properties of multicomponent CoCrCuFeNiTix alloys. *Intermetallics* **2007**, *15*, 357–362. [CrossRef]
38. Anderson, I.S.; McGreevy, R.L.; Bilheux, H.Z. Neutron Imaging and Applications. 2009. ISBN 978-0-387-78692-6. Available online: https://link.springer.com/book/10.1007/978-0-387-78693-3#about (accessed on 22 December 2017).